DISCOVERY AND MASS MEASUREMENTS OF A COLD, 10 EARTH MASS PLANET AND ITS HOST STAR

Y. Muraki[1,66], C. Han[2,67,68], D. P. Bennett[3,66,68,69], D. Suzuki[4,66], L. A. G. Monard[5,67], R. Street[6,70], U. G. Jorgensen[7,71], P. Kundurthy[8], J. Skowron[9,67], A. C. Becker[8], M. D. Albrow[10,69], P. Fouqué[11,69], D. Heyrovský[12], R. K. Barry[13], J.-P. Beaulieu[14,69], D. D. Wellnitz[15], I. A. Bond[16,66], T. Sumi[4,17,66], S. Dong[18,67,72], B. S. Gaudi[9,67], D. M. Bramich[19,70], M. Dominik[20,70,71,73],

AND

F. Abe[4], C. S. Botzler[21], M. Freeman[21], A. Fukui[4], K. Furusawa[4], F. Hayashi[4], J. B. Hearnshaw[10], S. Hosaka[4], Y. Itow[4], K. Kamiya[4], A. V. Korpela[22], P. M. Kilmartin[23], W. Lin[16], C. H. Ling[16], S. Makita[4], K. Masuda[4], Y. Matsubara[4], N. Miyake[4], K. Nishimoto[4], K. Ohnishi[24], Y. C. Perrott[21], N. J. Rattenbury[25], To. Saito[26], L. Skuljan[16], D. J. Sullivan[22], W. L. Sweatman[16], P. J. Tristram[23], K. Wada[1], P. C. M. Yock[21]
(THE MOA COLLABORATION)
G. W. Christie[27], D. L. DePoy[28], E. Gorbikov[29], A. Gould[9], S. Kaspi[29], C.-U. Lee[30], F. Mallia[31], D. Maoz[29], J. McCormick[32], D. Moorhouse[33], T. Natusch[27], B.-G. Park[30], R. W. Pogge[9], D. Polishook[34], A. Shporer[29], G. Thornley[33], J. C. Yee[9]
(THE μFUN COLLABORATION)
A. Allan[35], P. Browne[20,70], K. Horne[20], N. Kains[19], C. Snodgrass[36,37,70], I. Steele[38], Y. Tsapras[6,39]
(THE ROBONET COLLABORATION)
V. Batista[14], C. S. Bennett[40], S. Brillant[36], J. A. R. Caldwell[41], A. Cassan[14], A. Cole[42], R. Corrales[14], CH. Coutures[14], S. Dieters[42], D. Dominis Prester[43], J. Donatowicz[44], J. Greenhill[42], D. Kubas[14,36], J.-B. Marquette[14], R. Martin[45], J. Menzies[46], K. C. Sahu[47], I. Waldman[48], A. Williams[45], M. Zub[49]
(THE PLANET COLLABORATION)
H. Bourhrous[50], Y. Matsuoka[51], T. Nagayama[51], N. Oi[52], Z. Randriamanakoto[46]
(IRSF OBSERVERS)
V. Bozza[53,54], M. J. Burgdorf[55,56], S. Calchi Novati[53], S. Dreizler[57], F. Finet[58], M. Glitrup[65], K. Harpsøe[7], T. C. Hinse[7,30], M. Hundertmark[57], C. Liebig[20], G. Maier[49], L. Mancini[53,59], M. Mathiasen[7], S. Rahvar[60], D. Ricci[58], G. Scarpetta[53,54], J. Skottfelt[7], J. Surdej[58], J. Southworth[61], J. Wambsganss[49], F. Zimmer[49]
(THE MiNDSTEp CONSORTIUM)
A. Udalski[62], R. Poleski[62], Ł. Wyrzykowski[62,63], K. Ulaczyk[62], M. K. Szymański[62], M. Kubiak[62], G. Pietrzyński[62,64], AND I. Soszyński[62]
(THE OGLE COLLABORATION)

[1] Department of Physics, Konan University, Nishiokamoto 8-9-1, Kobe 658-8501, Japan
[2] Department of Physics, Chungbuk National University, 410 Seongbong-Rho, Hungduk-Gu, Chongju 371-763, Republic of Korea; cheongho@chungbuk.ac.kr
[3] Department of Physics, 225 Nieuwland Science Hall, University of Notre Dame, Notre Dame, IN 46556, USA; bennett@nd.edu
[4] Solar-Terrestrial Environment Laboratory, Nagoya University, Nagoya, 464-8601, Japan
[5] Bronberg Observatory, Centre for Backyard Astrophysics, Pretoria, South Africa
[6] Las Cumbres Observatory Global Telescope Network, 6740 Cortona Dr., Suite 102, Goleta, CA 93117, USA
[7] Niels Bohr Institute and Centre for Stars and Planet Formation, Juliane Mariesvej 30, 2100 Copenhagen, Denmark
[8] Astronomy Department, University of Washington, Seattle, WA 98195, USA
[9] Department of Astronomy, Ohio State University, 140 West 18th Avenue, Columbus, OH 43210, USA
[10] Department of Physics and Astronomy, University of Canterbury, Private Bag 4800, Christchurch 8020, New Zealand
[11] IRAP, CNRS, Université de Toulouse, 14 avenue Edouard Belin, 31400 Toulouse, France
[12] Institute of Theoretical Physics, Charles University, V Holešovičkách 2, 18000 Prague, Czech Republic
[13] Goddard Space Flight Center, Greenbelt, MD 20771, USA
[14] Institut d'Astrophysique de Paris, F-75014, Paris, France
[15] Department of Astronomy, University of Maryland, College Park, MD 20742, USA
[16] Institute for Information and Mathematical Sciences, Massey University, Private Bag 102-904, Auckland 1330, New Zealand
[17] Department of Earth and Space Science, Osaka University, 1-1 Machikaneyama-cho, Toyonaka, Osaka 560-0043, Japan
[18] Institute for Advanced Study, Einstein Drive, Princeton, NJ 08540, USA
[19] European Southern Observatory, Karl-Schwarzschild-Straße 2, 85748 Garching bei München, Germany
[20] SUPA, School of Physics & Astronomy, University of St Andrews, North Haugh, St Andrews, KY16 9SS, UK
[21] Department of Physics, University of Auckland, Private Bag 92-019, Auckland 1001, New Zealand
[22] School of Chemical and Physical Sciences, Victoria University, Wellington, New Zealand
[23] Mt. John University Observatory, P.O. Box 56, Lake Tekapo 8770, New Zealand
[24] Nagano National College of Technology, Nagano 381-8550, Japan
[25] Jodrell Bank Observatory, The University of Manchester, Macclesfield, Cheshire SK11 9DL, UK
[26] Tokyo Metropolitan College of Aeronautics, Tokyo 116-8523, Japan
[27] Auckland Observatory, P.O. Box 24-180, Auckland, New Zealand
[28] Department of Physics, Texas A&M University, 4242 TAMU, College Station, TX 77843-4242, USA
[29] School of Physics and Astronomy, Raymond and Beverley Sackler Faculty of Exact Sciences, Tel-Aviv University, Tel Aviv 69978, Israel
[30] Korea Astronomy and Space Science Institute, 776 Daedukdae-ro, Yuseong-gu 305-348 Daejeon, Republic of Korea
[31] Campo Catino Austral Observatory, San Pedro de Atacama, Chile
[32] Farm Cove Observatory, 2/24 Rapallo Place, Pakuranga, Auckland 1706, New Zealand
[33] Kumeu Observatory, Kumeu, New Zealand

³⁴ Benoziyo Center for Astrophysics, Weizmann Institute of Science, Rehovot 76100, Israel
³⁵ School of Physics, University of Exeter, Stocker Road, Exeter EX4 4QL, UK
³⁶ European Southern Observatory, Casilla 19001, Vitacura 19, Santiago, Chile
³⁷ Max-Planck-Institut fr Sonnensystemforschung, Katlenburg-Lindau, Germany
³⁸ Astrophysics Research Institute, Liverpool John Moores University, Twelve Quays House, Egerton Wharf,
Birkenhead CH41 1LD, UK
³⁹ Astronomy Unit, School of Mathematical Sciences, Queen Mary, University of London, London E1 4NS, UK
⁴⁰ Department of Physics, Massachusetts Institute of Technology, 77 Mass. Ave., Cambridge, MA 02139, USA
⁴¹ McDonald Observatory, 16120 St Hwy Spur 78 #2, Fort Davis, TX 79734, USA
⁴² School of Mathematics and Physics, University of Tasmania, Private Bag 37, Hobart, TAS 7001, Australia
⁴³ Department of Physics, University of Rijeka, Omladinska 14, 51000 Rijeka, Croatia
⁴⁴ Technische Universitaet Wien, Wieder Hauptst. 8-10, A-1040 Wienna, Austria
⁴⁵ Perth Observatory, Walnut Road, Bickley, Perth 6076, WA, Australia
⁴⁶ South African Astronomical Observatory, P.O. Box 9, Observatory 7925, South Africa
⁴⁷ Space Telescope Science Institute, 3700 San Martin Drive, Baltimore, MD 21218, USA
⁴⁸ Department of Physics and Astronomy, University College London, Gower Street, London WC1E 6BT, UK
⁴⁹ Astronomisches Rechen-Institut, Zentrum für Astronomie der Universität Heidelberg, Mönchhofstrasse 12-14,
69120 Heidelberg, Germany
⁵⁰ Department of Mathematics and Applied Mathematics, University of Cape Town, Rondebosch 7701, Cape Town, South Africa
⁵¹ Graduate School of Science, Nagoya University, Furo-cho, Chikusa-ku, Nagoya 464-8602, Japan
⁵² Department of Astronomical Science, The Graduate University for Advanced Studies (Sokendai), Mitaka, Tokyo 181-8588, Japan
⁵³ Department of Physics, University of Salerno, Via Ponte Don Melillo, 84084 Fisciano (SA), Italy
⁵⁴ Istituto Nazionale di Fisica Nucleare, Sezione di Napoli, Italy
⁵⁵ SOFIA Science Center, NASA Ames Research Center, Mail Stop N211-3, Moffett Field, CA 94035, USA
⁵⁶ Deutsches SOFIA Institut, Universitaet Stuttgart, Pfaffenwaldring 31, 70569 Stuttgart, Germany
⁵⁷ Institut fur Astrophysik, Georg-August-Universitat, Friedrich-Hund-Platz 1, 37077 Gottingen, Germany
⁵⁸ Institut dAstrophysique et de Geophysique, Allee du 6 Aout 17, Sart Tilman, Bat. B5c, 4000 Liege, Belgium
⁵⁹ Max Planck Institute for Astronomy, Königstuhl 17, 69117 Heidelberg, Germany
⁶⁰ Department of Physics, Sharif University of Technology, and School of Astronomy, IPM, 19395-5531 Tehran, Iran
⁶¹ Astrophysics Group, Keele University, Staffordshire ST5 5BG, UK
⁶² Warsaw University Observatory, Al. Ujazdowskie 4, 00-478 Warszawa, Poland
⁶³ Institute of Astronomy, University of Cambridge, Madingley Road, Cambridge CB3 0HA, UK
⁶⁴ Universidad de Concepción, Departamento de Astronomia, Casilla 160–C, Concepción, Chile
⁶⁵ Department of Physics & Astronomy, Aarhus University, Ny Munkegade 120, 8000 Arhus C, Denmark

ABSTRACT

We present the discovery and mass measurement of the cold, low-mass planet MOA-2009-BLG-266Lb, performed with the gravitational microlensing method. This planet has a mass of $m_p = 10.4 \pm 1.7\,M_\oplus$ and orbits a star of mass $M_\star = 0.56 \pm 0.09\,M_\odot$ at a semimajor axis of $a = 3.2^{+1.9}_{-0.5}$ AU and an orbital period of $P = 7.6^{+7.7}_{-1.5}$ yrs. The planet and host star mass measurements are enabled by the measurement of the microlensing parallax effect, which is seen primarily in the light curve distortion due to the orbital motion of the Earth. But the analysis also demonstrates the capability to measure the microlensing parallax with the *Deep Impact* (or *EPOXI*) spacecraft in a heliocentric orbit. The planet mass and orbital distance are similar to predictions for the critical core mass needed to accrete a substantial gaseous envelope, and thus may indicate that this planet is a "failed" gas giant. This and future microlensing detections will test planet formation theory predictions regarding the prevalence and masses of such planets.

Key words: gravitational lensing: micro – planetary systems

1. INTRODUCTION

In the leading core accretion planet formation model (Lissauer 1993), a key role is played by the "snow line," where the protoplanetary disk becomes cold enough for ices to condense. The timescale for agglomeration of small bodies into protoplanets is shortest just beyond the snow line because this is where the surface density of solid material is highest. The largest

protoplanets in these regions are expected to quickly reach a mass of $\sim 10\,M_\oplus$ by accumulating the majority of the solid material in their vicinity. They then slowly accrete a gaseous envelope of hydrogen and helium. The envelope can no longer maintain hydrostatic equilibrium when it reaches the mass of the core, so it collapses, starting a rapid gas accretion phase that leads to a massive giant planet. The hydrostatic accretion phase is predicted to have a much longer duration than the other two phases of solid accretion and rapid gas accretion (Pollack et al. 1996). This has several possible implications, including a higher frequency of low-mass, rocky/icy planets compared to gas giants, a feature in the final mass function of planets near the critical core mass of $\sim 10\,M_\oplus$, a relative paucity of planets with masses of 10–100 $M_\oplus$ (Ida & Lin 2004), and the formation of very few gas giants orbiting low-mass hosts (Laughlin et al. 2004), where the gas disks are expected to dissipate before the critical core mass is reached.
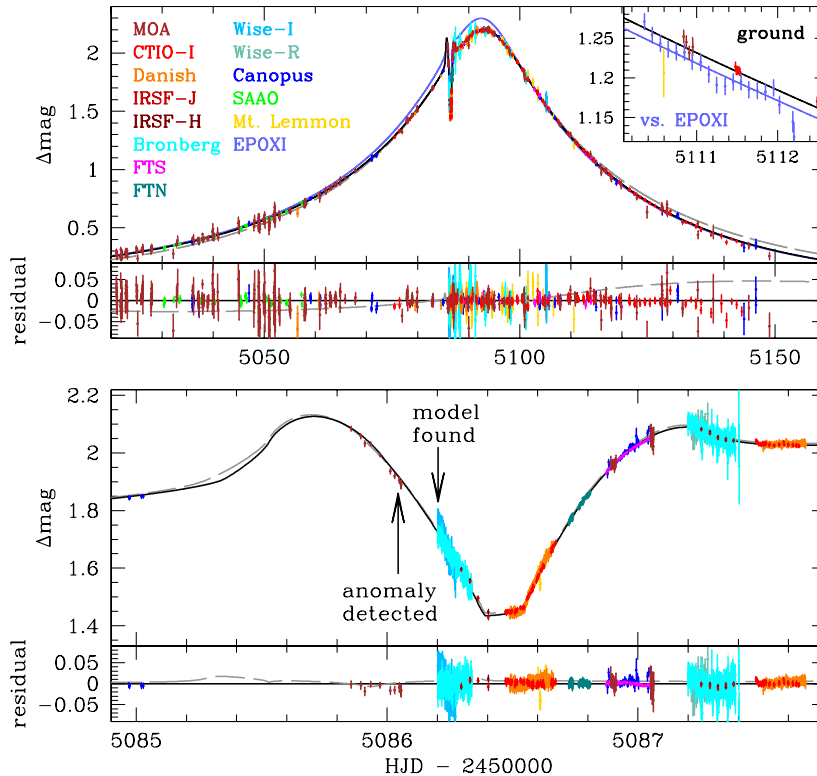

Figure 1. Data and best-fit model of the MOA-2009-BLG-266 microlensing event plotted with respect to magnitude of the unmagnified source. The upper panel shows the part of the microlensing light curve magnified by more than 25% and the lower panel shows a close-up of the planetary deviation. The sub-panel at the bottom of each panel shows the residual to the best-fit model, which is given by the solid black curves. The light-blue curve in the top panel is the model light curve for the position of the *EPOXI* spacecraft and the inset shows the data-binned *EPOXI* photometry from the ∼2 day period of observations from the *EPOXI*/HRI instrument. The gray dashed curve in each panel is the best-fit non-parallax microlensing model.

These predictions follow from general physical considerations, but they also rely upon a number of simplifying assumptions that make the calculations tractable. Therefore, they could be incorrect. For example, recent work suggests that uncertainties in the initial surface density of solids in the protoplanetary disk, grain opacities in protoplanetary atmospheres, and the size distribution of accreting planetesimals can radically alter the timescales of these various phases and thus the resulting distribution of final planet masses (Rafikov 2011; Hubickyj et al. 2005; Movshovitz & Podolak 2008). Therefore, the measurement of the mass function of planets down to below the predicted critical core mass will provide important constraints on the physics of planet formation.

Attempts to test core accretion theory predictions with the mass distribution of the ∼500 detected exoplanets and the ∼1200 candidate exoplanets found by the *Kepler* mission (Borucki et al. 2011) have met with varied success. Radial velocity detections confirm the prediction that massive gas giants should be rare around low-mass stars (Johnson et al. 2010), but the prediction that 10–100 $M_\oplus$ planets should be rare in short-period orbits is contradicted by the data (Howard et al. 2010). *Kepler* finds a large population of planets at ∼2.5 $R_\oplus$ in short-period orbits, which is consistent with a result from the radial velocity planet detection method (Howard et al. 2010). This might be considered a confirmation of the core accretion theory prediction that ∼10 $M_\oplus$ "failed gas giant core" planets should be common, but in fact all of the low-mass planets found by radial velocity and transit methods have been well interior to the snow line, where these "failed core" planets are thought to form. It is possible that the exoplanet mass (or radius) function is quite different outside the snow line due to such

processes as sorting by mass through migration (Ward 1997) and photoevaporation of gaseous envelopes (Baraffe et al. 2005). Thus, a study of the exoplanet mass function beyond the snow line should provide a sharper test of the core accretion theory.

The gravitational microlensing method (Mao & Paczyński 1991; Bennett 2008; Gaudi 2010) has demonstrated sensitivity extending down to planets of mass <10 $M_\oplus$ in orbits beyond the snow line (Bennett & Rhie 1996; Beaulieu et al. 2006; Bennett et al. 2008). Thus, it can provide a complementary probe of the physics of planet formation for planets that have migrated little from their putative birth sites. A statistical analysis of some of the first microlensing discoveries (Gould et al. 2010) indicates that cold, Saturn-mass planets beyond the snow line are more common than gas giants found in closer orbits with the Doppler radial velocity method (Cumming et al. 2008). Another microlensing study (Sumi et al. 2010) of the mass function slope showed that planets of ∼10 $M_\oplus$ are even more common than these cold Saturns, in general agreement with the core accretion theory prediction for "failed gas giant cores" (Kennedy & Kenyon 2008; Thommes et al. 2008).

A well-sampled planetary microlensing light curve provides a direct determination of the planet:star mass ratio, but not the individual masses of planet and host star. Furthermore, planets found by microlensing typically have distant, low-mass host stars, so their faintness makes them difficult to characterize. While finite source effects in the light curve do constrain a combination of the mass and distance, it has often been necessary to estimate the planet and host masses and distance with a Bayesian analysis (Beaulieu et al. 2006) based on a Galactic model and prior assumptions about the exoplanet distribution. When the masses of planetary microlenses and their

host stars can be measured, they will provide tighter constraints on planet formation theory.

Here, we present the first example of a mass measurement for a cold, low-mass planet discovered by microlensing, which has a mass very similar to the expected critical mass for gas accretion. The light curve of microlensing event MOA-2009-BLG-266 exhibits a planetary signal due to a companion with a mass ratio of $\sim 6 \times 10^{-5}$ (see Figure 1). The light curve also reveals a microlensing parallax signal due to the orbital motion of the Earth (Gould 1992; Alcock et al. 1995). When combined with the information from the finite size of the source during the planetary perturbation, this allows one to work out the complete geometry of the microlensing event (Gould 1992), yielding a measurement of the host and planet masses. This has been done previously at this level of precision only for the giant planets in the system OGLE-2006-BLG-109L (Gaudi et al. 2008; Bennett et al. 2010). In addition, observations from the *EPOXI* spacecraft in a heliocentric orbit corroborate the mass measurement for MOA-2009-BLG-266Lb, and demonstrate the potential of obtaining masses for planetary events that are too brief for a parallax measurement due to Earth's orbit.

Our observations are described in Section 2, and Section 3 details our data reduction procedures. Section 4 presents a detailed discussion of the source star properties, and we discuss the determination of the properties of the planetary system in Section 5. Finally, we discuss some of the implications of this discovery in Section 6.

2. OBSERVATIONS

The microlensing event MOA-2009-BLG-266 [(R.A., decl.) $= (17^h48^m05^s95, -35°00'19''48)$ and $(l, b) = (-4°9, -3°6)$] was discovered on 2009 June 1 by the Microlensing Observations in Astrophysics (MOA) collaboration MOA-II 1.8 m survey telescope at Mt. John University Observatory in New Zealand. The Probing Lensing Anomalies NETwork (PLANET), Microlensing Follow-Up Network (μFUN), and Microlensing Network for the Detection of Small Terrestrial Exoplanets (MiNDSTEp) teams followed some of the early part of the light curve. The wide field of view (FOV; 2.2 deg^2) of the MOA-II survey telescope allows MOA to monitor the Galactic bulge with a high enough cadence to discover planetary signals in any of the 500–600 microlensing events they discover every year, and this has resulted in the discovery of several exoplanets (Sumi et al. 2010; Bennett et al. 2008). On 2009 September 11, the MOA survey detected such an anomaly in the MOA-2009-BLG-266 light curve and announced it as a probable planetary anomaly. In response to the alert, the event was intensively observed using the combined telescopes of the μFUN, PLANET, RoboNet, and MiNDSTEp teams, resulting in nearly complete light curve coverage for the last $\sim$75% of the anomaly. Within four hours, modeling by MOA confirmed that this was almost certainly a planetary event, which led to observations by the InfraRed Survey Telescope (IRSF) at the South African Astronomical Observatory (SAAO). This and further modeling by MOA and μFUN, as well as rapid reduction of μFUN data prevented observing resources from being diverted to other interesting events that were found the same day.

Our data set consists of observations from 13 different telescopes, with several telescopes contributing data in different passbands. We treat each telescope–passband combination as an independent data set with independent flux parameters in the microlensing light-curve fits, and this combined data set includes 18 telescope–passband combinations. The planetary

signal was first seen in data from the MOA-II 1.8 m survey telescope (Sako et al. 2008) at Mt. John University Observatory in New Zealand. This analysis includes 1996 MOA-II observations taken from 2007 to 2009.

In response to the MOA-II microlensing event alert on 2009 June 1 and the microlensing anomaly alert on 2009 September 11, data were obtained from a number of follow-up groups. The PLANET collaboration (Beaulieu et al. 2006) added this event to its target list for the 1.0 m telescope at Mt. Canopus Observatory near Hobart, Australia, and the 1.0 m telescope at SAAO on 2009 July 16 as a regular planet search target following the alert plus follow-up planet detection strategy (Gould & Loeb 1992). Unfortunately, the PLANET observing time allocation at SAAO ended on 2009 August 18, which was nearly a month prior to the planetary signal. Additional observations prior to the detection of the planetary anomaly were also obtained from μFUN-CTIO, MiNDSTEp-Danish, and Robonet-Faulkes South. These observations help to constrain the microlensing parallax signal, but the parallax signal is primarily detected in the MOA data.

Canopus had 35 observations spanning 49 days prior to the planetary signal, including four observations on the night prior to the beginning of the planetary signal. MOA had no observations on the two days prior to the beginning of the planetary anomaly, so the Canopus data were the only observations taken on the night before the planetary anomaly began. These observations indicated no deviation from a single-lens light curve, and this indicated that the anomaly had a very short duration, as is typical for light curve deviations due to low-mass planets. Thus, the Canopus data contributed to the identification of the planetary nature of the anomaly identified in the MOA data. This was important because another anomalous event and a high-magnification event were also identified by MOA on the same day. The final data set contains 205 *I*-band observations from Canopus and 33 *I*-band observations from SAAO.

The first data in response to MOA's 2009 September 11 alert on the planetary anomaly came from the μFUN group with observations from the 0.4 m telescope Bronberg Observatory in Pretoria, South Africa and the 1.0 m telescope of Wise Observatory in Israel, which were able to begin observations $\sim$4 hr after the anomaly alert (which coincided with the last MOA observation on the night of the alert). About two hours later (after the MOA planetary light curve model had been circulated), a series of observations were begun with the 1.4 m IRSF, which is located at SAAO and features simultaneous imaging in the *J*, *H*, and *K* bands. The final data set includes 597 unfiltered observations from Bronberg, 36 and 30 observations in *I* and *R* (respectively) from Wise, and 19, 20, and 18 observations in the *J*, *H*, and *K* bands from IRSF. The raw Bronberg data consist primarily of very densely sampled observations during the two nights of the planetary deviation, and the 1705 observations from Bronberg were binned to a 7.2 minute cadence to yield the 597 measurements that were used for all the light curve modeling. The IRSF observations are much sparser, but they do include coverage of the first caustic crossing endpoint, as well as observations from 2010 March, when the microlensing magnification was <1.01.

The μFUN group also obtained a large number of observations in the *H*, *I*, and *V* bands from the ANDICAM instrument on the 1.3 m SMARTS telescope at CTIO in Chile. This instrument observes simultaneously in the optical and infrared, so the final data set includes 861 *H*-band observations, which mostly overlap in time with the 317 *I*-band and 56 *V*-band observations

that are included in the final data set. The CTIO data also include regular sampling of the stellar microlensing light curve after the planetary anomaly and a few images from 2010, so they contribute significantly to the microlensing parallax constraints. The MiNDSTEp group also obtained dense light curve coverage of the planetary deviation using the 1.54 m Danish Telescope at the European Southern Observatory in La Silla, Chile, and their data set consists of 611 I-band observations. Another μFUN telescope in the Americas was the 1.0 m telescope at Mt. Lemmon Observatory in Arizona, which contributed 73 I-band observations to the final data set.

The rise of the light curve from the planetary magnification "trough" was covered largely by the 2.0 m Faulkes telescopes operated by the Las Cumbres Global Telescope Network (LCOGTN). The Faulkes North telescope (FTN) located in Haleakala, Hawaii contributed 148 SDSS I-band observations to the final data set, while the Faulkes South Telescope (FTS) located in Siding Springs, Australia, contributed 128 SDSS I-band observations to the final data set. The Canopus and MOA telescopes also covered the last part of the rise from the light curve "trough"

The Robonet group also obtained a substantial amount of FTS data in the SDSS g, r and Pan-STARRS z and y with 52, 51, 49, and 115 images in each passband, respectively. This multicolor data was obtained because it was thought that it might be helpful to help calibrate the unfiltered $EPOXI$ data.

Our complete light curve data set also includes 929 Optical Gravitational Lensing Experiment (OGLE)-III I-band observations that ended on 2009 May 3 with the termination of the OGLE-III survey, when the magnification was $A \approx 1.06$. (OGLE-III was terminated to enable an upgrade to a more sensitive camera with a larger FOV for the OGLE-IV survey.)

Finally, we obtained high angular resolution AO images from the NACO instrument on the European Southern Observatory's Very Large Telescope (VLT) facility in 2010 after the event was over.

3. DATA REDUCTION

Most of the photometry was done using the Difference Image Analysis (DIA) method (Tomaney & Crotts 1996). The MOA images were reduced with the MOA DIA pipeline (Bond et al. 2001), while the PLANET, RoboNet-II, MiNDSTEp, and most of the μFUN data were reduced with a DIA routine following the same basic strategy as ISIS (Alard & Lupton 1998), but using a numerical kernel (Bramich 2008). The implementation of this numerical kernel DIA routine that was used for most of the data was pySIS (version 3.0) (Albrow et al. 2009) but the Robonet pipeline was used for the FTS data (Bramich 2008). The OGLE data were reduced with the OGLE pipeline (Udalski 2003). The Mt. Lemmon data were reduced with DoPHOT (Schechter et al. 1993), and the IRSF data were reduced with SoDoPHOT, which was derived from DoPHOT (Bennett et al. 1993). SoDoPHOT was also used to reduce the CTIO I- and V-band data, but this SoDoPHOT reduction was only used to help calibrate the $EPOXI$ photometry. The multicolor FTS data and the CTIO data were also reduced with ALLFRAME (Stetson 1994) to aid the $EPOXI$ photometry calibration, but only the SoDoPHOT reductions of the CTIO I- and V-band data were used in the final $EPOXI$ calibrations. The pySIS reductions of the CTIO data were used for light curve modeling.

One difficulty that is sometimes encountered with DIA photometry is that excess photometric scatter can result for images where the target star is much brighter or much fainter

than it is in the reference frame. This effect was noticed in the pySIS reductions of the Canopus data. Therefore, the final Canopus photometry was a combination of two reductions based on reference frames in which the brightness of the target was very different. The relative normalization of these two reductions was determined by a linear fit with the 3σ outliers removed from each data set. Then the final Canopus photometry was determined by a weighted sum of these two data sets with the weighting determined by the difference between the target brightness in the image being reduced and the two reference frames.

An additional correction is necessary for the unfiltered Bronberg data. The color dependence of atmospheric extinction can give rise to systematic photometry errors because the color of the source star is typically slightly different from the color of the stars used to normalize the photometry. This gives rise to a photometry error that scales as the airmass for monochromatic light and a static atmosphere. For a very wide passband, like that of Bronberg, the effective passband depends on the amount of atmospheric extinction, so the photometric error does not follow the scaling with airmass very precisely (Stubbs et al. 2007). Furthermore, the amount of dust in the atmosphere can change with time. Hence, we correct the Bronberg photometry by normalizing the photometry of the target star to a set of stars with a similar color (Bennett et al. 2010).

The VLT/NACO data were reduced following the procedures used for the analysis of MOA-2007-BLG-192 (Kubas et al. 2011).

3.1. Reduction of EPOXI Data

For a period of just under three days on 2009 October 10–12, we were able to obtain observations using the High Resolution Instrument (HRI) visible imager on the $EPOXI$ (Christiansen et al. 2011) spacecraft when it was located $\sim$0.1 AU from Earth. Observations with the $EPOXI$ HRI were requested in an attempt to constrain the microlensing parallax effect and obtain precise mass measurements of the MOA-2009-BLG-266Lb planet and its host star. We could obtain these observations because our target field was able to provide a better test of newly installed pointing control software than a less dense stellar field.

The $EPOXI$ data consist of 4127 50 s exposures with the "clear-6" filter. To minimize data transfer requirements, the data were taken as 128×128 and 256×256 pixel sub-frames. The first 3375 exposures used 128×128 sub-frames, and the last 752 images were 256×256 sub-frames. However, the pointing stability was such that the target occasionally drifted out of the 128×128 sub-frames, and it was only possible to do photometry on 2900 of these 3375 128×128 pixel images. An example of one of these 128×128 pixel images is shown on the right side of Figure 2.

The instrumental point-spread function (PSF) of the HRI on the *Deep Impact* probe is strongly dependent on the color of the target star. In addition, the instrument is permanently defocused, yielding a toroidal-shaped PSF. This is clearly not optimal for crowded field photometry, which typically requires a spatially varying empirical PSF model for deblending. Since we performed photometry using the Daophot/Allstar/Allframe software suite (Stetson 1994), we first required a model of the instrumental PSF that is usable by Daophot.

Instrumental PSFs have been generated by Barry (2010) for the HRI using the Drizzle algorithm (Fruchter & Hook 2002). In this process several hundred images of a standard star were added together to create a ten-time oversampled PSF
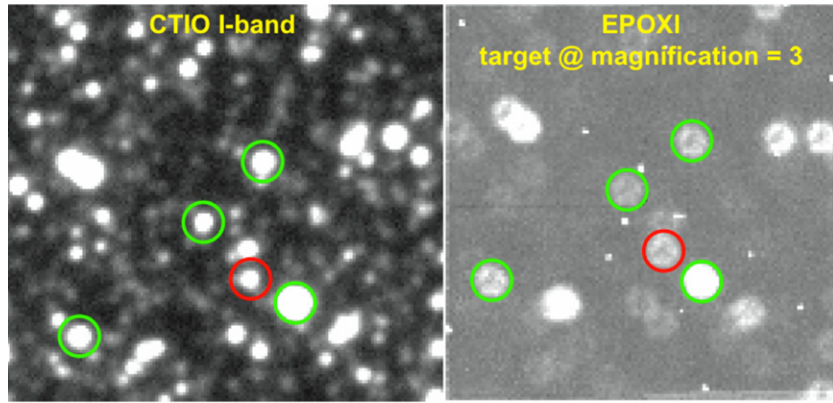
Figure 2. Comparison of CTIO *I*-band (left) and *EPOXI* (right) images of the MOA-2009-BLG-266 target, indicated by red circles. North is to the right and east is up in the CTIO image, and the *EPOXI* image is rotated slightly from this orientation. The green circles indicate the four photometry comparison stars, each having $V - I$ within 0.9 mag of the target star. The comparison stars also have only one star identified in the CTIO frames within $3''$ of the matched position of the *EPOXI* star.

model appropriate for that object. To approximate the PSF of MOA-2009-BLG-266, with $V - I = 1.82$, we co-added the instrumental PSFs of GJ436 with $V - I = 2.44$; and XO-2 with $V - I = 0.75$ with weightings of 0.795 and 0.205, respectively. This composite PSF was added to an otherwise empty image in a 3×3 grid, with each realization downsampled to standard resolution using a center pixel shifted by ± 5 pixels in x and/or y. Daophot was then run on this image, using all nine images to build its own internal, double-resolution PSF model using an empirical function plus "lookup table."

Approximately 1% of pixels in our 50 s observations contain signatures of cosmic rays. We filtered these pixels using an algorithm that identifies features sharper than expected from the PSF, through pairwise comparison of neighboring pixels. These pixels were masked and objects underneath these pixels ignored when generating light curves. We used Daophot to detect stars in each image, and then Allstar to perform joint PSF photometry on all stars in a given image. We generated a master starlist by matching the results of the Allstar analysis using Daomatch and Daomaster. This starlist was then sent to Allframe, which simultaneously photometered all images in a self-consistent manner with regard to centroiding and deblending.

To assemble the final light curves, we first aggregated the Allframe measurements of a given star across all images. Due to the difficulty of obtaining precise flat-field images in space, we cannot calibrate these images using the same methods as would be used for ground-based images. As a result, the light curves of all the stars observed by *EPOXI*/HRI show variations at the ~ 1% level on a timescale of a few hours, which is the time that it takes for the pointing to drift a distance of the order of the PSF FWHM. Because this is the dominant term in the *EPOXI*/HRI photometry errors, we bin the data at an interval of 2.4 hr, which seems to remove most, but not all, of the correlations. This gives the light curve shown in the inset in the upper right-hand corner of Figure 1.

We had also hoped to get *EPOXI*/HRI observations after the MOA-2009-BLG-266 microlensing event had returned to its baseline brightness in 2010 March or April. Unfortunately, the *EPOXI* operations team was busy with preparations for the 2010 November encounter with the comet Hartley 2, so no baseline observations were possible. Therefore, we have determined the baseline brightness in the *EPOXI* by comparing the *EPOXI* images to *V*- and *I*-band CTIO images taken in 2010 June, when the microlensing event had returned to baseline. The *I*-band CTIO image is compared to one of the *EPOXI* frames

in Figure 2. Because of the relatively large *EPOXI*/HRI PSF, we consider only stars in the *EPOXI* images that have only one counterpart star within a radius of $3''$ of the position of the *EPOXI* star. We also limit our consideration to stars within 0.9 mag of the $V - I$ color of the microlensed target star. There are four stars that satisfy this condition and appear in more than half of the images in which the target star appears. These are the four stars indicated by the green circles in Figure 2. We fit the mean "clear"-filter *EPOXI* magnitude, C_{EPOXI}, to the instrumental CTIO magnitudes from the SoDoPHOT reductions, and this yields the following linear relationship between the average *EPOXI* magnitudes and CTIO magnitudes,

$$C_{EPOXI} = 0.520 I_{\text{CTIO}} + 0.480 V_{\text{CTIO}}. \tag{1}$$

The fit to the magnitude of these four comparison stars gives $\chi^2 = 0.22$ for 2 degrees of freedom if the uncertainty in the *EPOXI* magnitudes is assumed to be 0.004 mag. We use this formula to determine the baseline C_{EPOXI} magnitude, and we add this to the light curve as a final measurement with an assumed uncertainty of 0.01 mag.

We note that this calibration procedure for the *EPOXI* data is probably more reasonably considered to be a procedure to calibrate the source star flux instead of the baseline brightness, which includes the brightness of any unresolved stars blended with the source. But we chose to treat the unmagnified flux estimate as an estimate of the baseline brightness as this is more conservative.

4. SOURCE STAR PROPERTIES AND EINSTEIN RADIUS

Planetary microlensing events typically have caustic crossing or cusp approach features that resolve the finite angular size of the source star, and MOA-2009-BLG-266 is no exception as it has clear caustic crossing features. The modeling of such features constrains the source radius crossing time, $t_\star$, and this can be quite useful because $t_\star$ can be used to determine the angular Einstein radius, $\theta_E = \theta_\star t_E / t_\star$, as long as the source star angular radius, $\theta_\star$, can be determined. In events such as MOA-2009-BLG-266, with a strong microlensing parallax signal, θ_E can be combined with the parallax measurement to yield the lens system mass. Therefore, it is important to make an accurate determination of the angular radius of the source star, $\theta_\star$.
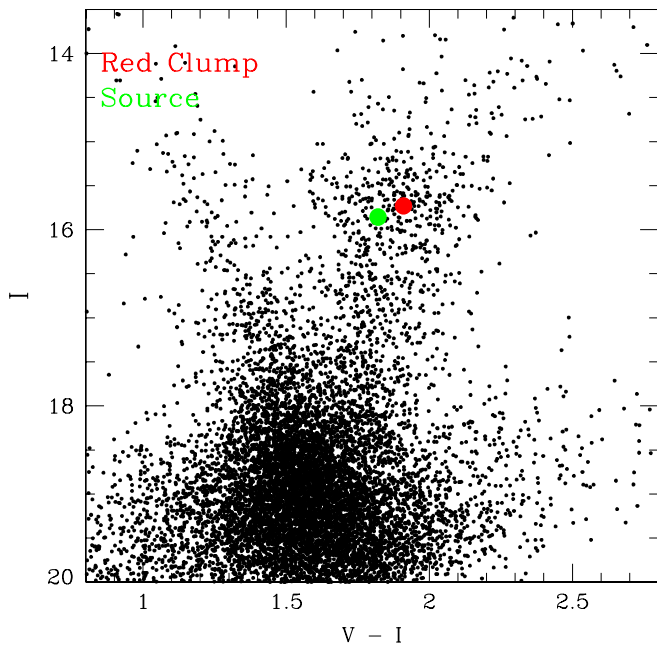
Figure 3. Color–magnitude diagram of stars from the OGLE-III database within 2′ of the MOA-2009-BLG-266 source star. The center of the red clump and the source star are indicated by the red and green spots.

Figure 4. $I - H$ color–magnitude diagram of stars within 2′ of the MOA-2009-BLG-266 source star, based on IRSF H-band data calibrated to 2MASS and OGLE-III I-band photometry. As in Figure 3, the red and green spots indicate the red clump center and the source star.

4.1. Source Star Colors and Extinction

The angular radius of the source star can be determined from its brightness and color, once the effect of interstellar extinction has been removed. We start from the CTIO V- and I-band magnitudes and the IRSF H-band magnitude that have been determined from the best-fit model. The V- and I-band magnitudes have been calibrated to the OGLE-III system (Udalski et al. 2008) and the IRSF H band has been calibrated to the Two Micron All Sky Survey (2MASS; Carpenter 2001).[74] The comparison between the 2MASS and the IRSF H-band data is subject to complications due to variability and blending, because the 2MASS images, with their 2″ pixels, have significantly worse angular resolution than IRSF. This means that many of the apparent 2MASS "stars" cannot be used for the calibrations because they are actually blended images of two or more stars that are resolved in the IRSF images. This makes calibration of the CTIO H-band images difficult, because of the relatively small 5.5 arcmin² CTIO H FOV. Fortunately, the IRSF FOV is ∼60 arcmin², and it is possible to use over 400 unblended 2MASS stars for the H-band calibration. These calibrations combined with the best-fit light-curve models yield source magnitudes of

$$H_s = 13.780 \pm 0.030, \tag{2}$$

$$I_s = 15.856 \pm 0.030, \tag{3}$$

and

$$V_s = 17.677 \pm 0.030, \tag{4}$$

where the uncertainties are almost entirely due to the calibrations (including the uncertainty in the OGLE-III calibration). These magnitudes are indicated by the green dots in the color–magnitude diagrams shown in Figures 3 and 4. The fit
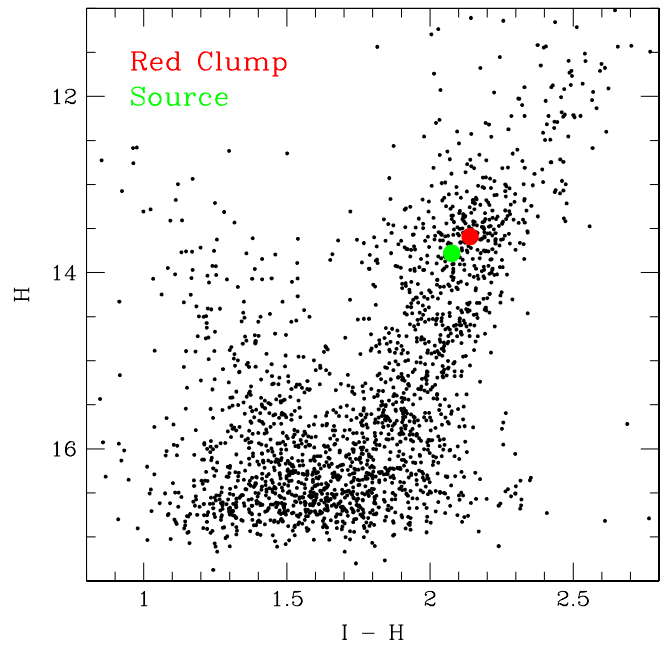
[74] Improved calibrations are available at
http://www.ipac.caltech.edu/2mass/releases/allsky/doc/sec6_4b.html.

uncertainties are ⩽0.005 mag in all three passbands, and the $u_0 > 0$ model predicts a source that is 0.005 mag brighter than the best-fit $u_0 < 0$ model.

4.2. Source Star Radius

We can use the magnitudes from Equations (2) to (4) to determine the source star angular radius, but first we must estimate the foreground extinction. We determine the source radius using the method of Bennett et al. (2010), which is a generalization to three colors of an earlier two-color method (Albrow et al. 2000). Following this procedure, we find the VIH magnitudes of the center of the red clump giant distribution to be

$$H_{rc} = 13.59 \pm 0.10, \tag{5}$$

$$I_{rc} = 15.73 \pm 0.10, \tag{6}$$

and

$$V_{rc} = 17.64 \pm 0.10, \tag{7}$$

for stars within 2′ of the source star. These are indicated by the red spots in Figures 3 and 4. Assuming a distance to the source of 8.8 kpc (Rattenbury 2007), we can use these red clump magnitudes to estimate the extinction, which we find to be $A_H = 0.36$, $A_I = 1.22$, and $A_V = 2.14$, following an $R_V = 2.77$ Cardelli et al. (1989) extinction law. These then yield de-reddened magnitudes of $H_{s0} = 13.42$, $I_{s0} = 14.64$, and $V_{s0} = 15.54$. Unlike the case for dwarf stars, the accuracy of the $V - I$, $V - H$, and $I - H$ surface-brightness–color relations (Kervella et al. 2004) is similar, but the $I - H$ relation yields an angular radius estimate that is almost completely independent of the reddening law, if it follows the Cardelli et al. extinction law (Cardelli et al. 1989), but this may be due to the fact that the A_I/A_H ratio does not vary much with this extinction law.

Table 1
Fit χ^2 Values

Passband	Data Points	Best Orb. Fit	Best No Orb. Fit	Lin.-LD No Orb. Fit
MOA-red*	1996	1983.79	1981.82	1983.57
FTS-SDSS-I*	128	121.15	127.36	130.52
Canopus-I*	205	205.84	204.46	205.96
Wise-I*	36	34.33	34.86	33.40
Wise-R*	30	27.82	27.83	27.84
Bronberg-un*	597	601.92	601.01	601.57
IRSF-K*	18	16.68	16.68	16.54
IRSF-H*	20	20.13	21.00	19.50
IRSF-J*	19	19.15	19.79	19.35
SAAO-I	33	32.58	32.59	32.60
CTIO-H*	861	862.57	862.26	853.64
CTIO-I*	317	309.42	308.68	309.61
CTIO-V*	56	56.08	56.08	56.49
Danish-I*	611	603.66	603.25	610.11
OGLE-I	929	920.60	920.70	920.70
Mt. Lemmon-I	73	71.01	70.97	71.26
FTN-SDSS-I*	148	144.76	145.18	149.17
EPOXI-un	21	18.68	18.88	18.87
Total	6098	6050.17	6053.41	6060.68

Note. Asterisks denote passbands using limb-darkening tables; "un" denotes unfiltered.

In any case, all three of these relations imply that the angular radius of the source star is

$$\theta_\star = 5.2 \pm 0.2 \ \mu\text{as.} \qquad (8)$$

This and the source radius crossing time of $t_\star = 0.326 \pm 0.007$ days imply that the relative lens-source proper motion and Einstein radius are

$$\mu_{\text{rel}} = \theta_\star / t_\star = 5.86 \pm 0.26 \ \text{mas yr}^{-1}, \qquad (9)$$

and

$$\theta_E = \mu_{\text{rel}} t_E = 0.98 \pm 0.04 \ \text{mas}, \qquad (10)$$

respectively.

4.3. Limb Darkening

During caustic crossings the lens effectively scans the source star with high angular resolution. As a result, the shape of the light curve reflects the underlying limb darkening of the star (Witt 1995; Bennett & Rhie 1996). Hence, in order to analyze caustic-crossing events such as MOA-2009-BLG-266, one needs to account for the limb darkening appropriately. For the previous planetary microlensing events (Bond et al. 2004; Udalski et al. 2005; Beaulieu et al. 2006; Gould et al. 2006; Gaudi et al. 2008; Bennett et al. 2008; Dong et al. 2009b; Sumi et al. 2010; Janczak et al. 2010; Miyake et al. 2011; Batista et al. 2011), limb darkening has generally been treated within the linear limb-darkening approximation. In some cases, the two-parameter square-root limb-darkening law was used (Dong et al. 2009b; Janczak et al. 2010), even though there has been no indication that the details of the limb-darkening treatment had any noticeable effect on the other model parameters for a planetary microlensing event.

In the case of MOA-2009-BLG-266, there was reason to suspect that the treatment of limb darkening could be important. This is because, as we discuss below in Section 5.1, there are two approximately degenerate microlensing parallax models that have slightly different binary lens parameters. The source crosses the caustics at a slightly different angle for the two

models. This suggests that the detailed treatment of limb darkening might have some influence on the difference in χ^2 between these two degenerate models. As shown by Heyrovsky (2007), using linear limb darkening may introduce photometric errors at the level of 0.01 due to the approximation itself and the choice of method used for computing the linear model coefficients. In order to avoid introducing any such inaccuracies in the analysis of the event, we directly use the limb-darkening profile from a theoretical model atmosphere of the source star, instead of its analytical approximations.

Based on the location of the source star on the color–magnitude diagram, we assume a temperature of $T_{\text{eff}} \approx 4750$ K, surface gravity of $\log g = 2.5$, and solar metallicity. We use a model atmosphere from Kurucz's ATLAS9 grid (Kurucz 1996, 1993a, 1993b)[75] corresponding to these parameters. The raw model data provide values of the specific intensity as a function of wavelength for 17 different positions on the stellar disk. In order to obtain the light-curve-specific limb-darkening profile, we integrate the specific intensity over the relevant filter passband, weighted by the filter transmission, the quantum efficiency of the CCD, and interstellar extinction (see Section 4.1). In order to compute the limb darkening at an arbitrary position on the stellar disk, we interpolate the obtained points using cubic splines with natural boundary conditions (Heyrovsky 2003, 2007). The light-curve-modeling code uses pre-computed tabulated intensity values for a sufficiently dense spacing of radial positions on the stellar disk.

This approach avoids a potential source of low-level systematic error without any degrees of freedom to the model. In Table 1 we compare the results of our analysis with those obtained by the usual approach, using linear limb-darkening coefficients from Claret (2000). For the parameters of the source star Claret (2000) provides coefficient values $u_\lambda = 0.7844, 0.7035, 0.6087, 0.4868, 0.4181$, and 0.358 for the V, R, I, J, H, and K_s passbands, respectively. Tabulated intensity values give a χ^2 improvement over the linear approximation of $\Delta\chi^2 = 7.27$ for the best-fit static models without orbital motion. Therefore, the

---

[75] Updated online at http://kurucz.harvard.edu.

Table 2
Best-fit Parameters

Parameter	Units	Best Orb.	MCMC Orb.	Best No Orb.	MCMC No Orb.
χ^2/dof		6050.17		6053.41	
t_E	days	61.447	61.47 ± 0.40	61.612	61.54 ± 0.36
t_0	HJD$'$	5093.257	5093.257 ± 0.083	5093.298	5093.285 ± 0.051
u_0		0.13158	0.1315 ± 0.0008	0.13129	0.1314 ± 0.0008
s		0.91429	0.91434 ± 0.00036	0.91425	0.91421 ± 0.00036
q	10^{-5}	5.815	5.63 ± 0.25	5.425	5.45 ± 0.07
θ	rad	2.2677	2.2692 ± 0.0034	2.2715	2.2708 ± 0.0035
$t_\star$	days	0.33140	0.3262 ± 0.0068	0.32152	0.3216 ± 0.0012
π_E		0.2094	0.223 ± 0.037	0.2395	0.232 ± 0.038
ϕ_E	rad	0.760	0.74 ± 0.16	0.640	0.70 ± 0.14
$\pi_{E,N}$		0.1517	0.1665 ± 0.0503	0.1921	0.1795 ± 0.0493
$\pi_{E,E}$		0.1442	0.1439 ± 0.0035	0.1430	0.1435 ± 0.0035
$\dot{s}_x$	10^{-3} day^{-1}	-0.34	-0.25 ± 0.15		
$\dot{s}_y$	10^{-3} day^{-1}	-2.05	-0.84 ± 1.49		
T_{orb}	days	2380			

Note. Parameters are given in an inertial geocentric frame fixed at HJD$' = 5086$ (HJD$' = $ HJD $- 2450{,}000$).

tabulated limb-darkening tables fit the data somewhat better, at least for the static lens case, but the implied planetary parameters do not change significantly.

5. PLANET CHARACTERIZATION AND MODELING

5.1. Modeling

The basic parameters for planetary events like MOA-2009-BLG-266 are straightforward to determine, as a reasonable estimate can be made from the single-lens parameters (found from a fit with the planetary deviation excluded) and inspection of the light curve (Gould & Loeb 1992). The main feature of the deviation is the half-magnitude decrease in magnification centered at HJD$' = 5086.5$. This indicates that a planet is perturbing the minor (saddle) image created by the stellar lens and that the star–planet separation is less than the Einstein radius. Such a light curve cannot be mimicked by non-planetary perturbations (Gaudi & Gould 1997). The basic planetary parameters can then be estimated following the arguments given in Sumi et al. (2010). In practice, this is not how the parameters were determined, however.

We model the data using standard methods (Bennett 2010; Dong et al. 2006) to extract the precise parameters and uncertainties of the light curve fit. It is convenient to describe microlensing events in terms of the Einstein ring radius, $R_E = \sqrt{(4GM_L/c^2)D_S x(1-x)}$, which is the radius of ring image seen when the source and (single) lens are in perfect alignment. Here M_L is the lens system mass, $x = D_L/D_S$, and D_L and D_S are the lens and source distances. Microlensing by a single lens, such as an isolated star, is described by three parameters: the Einstein radius crossing time, t_E, and the time, t_0, and distance (with respect to R_E), u_0, of closest alignment between the source and lens center of mass. Planetary microlensing events require three additional parameters: the planet/star mass ratio, q, the star–planet separation, s, in units of R_E, and angle of the source trajectory with respect to the star–planet axis, θ. The source radius crossing time, $t_\star$, is also required because, like most planetary events, MOA-2009-BLG-266 has sharp light curve features that resolve the angular size of the source star.

The MOA and Canopus data for the event were modeled immediately upon the detection of the planetary perturbation using the method of Bennett (2010), supplemented with the addition of the hexadecapole approximation (Pejcha & Heyrovsky 2009;

Gould 2008). This found the basic solution that we present here, plus a disfavored alternative $s > 1$ solution, which was excluded within hours when the planetary deviation data from South Africa, Israel, and Chile became available. The $s < 1$ solution was refined as more data came in, and the two degenerate solutions that we present here emerged when microlensing parallax was added to the modeling.

We also conducted a blind search of parameter space using the approach of Dong et al. (2006), where the binary parameters s, q, and θ are fixed at a grid of values, while the remaining parameters are allowed to vary so that the model light curve results in minimum χ^2 at each grid point. A Markov Chain Monte Carlo (MCMC) method was used for χ^2 minimization. Then, the best-fit model is obtained by comparing the χ^2 minima of the individual grid points.

5.2. Best-fit Model

The modeling indicates that the perturbation of MOA-2009-BLG-266 is produced by the crossing of a clump giant source star over the planetary caustic produced by a low-mass planet. As we discuss below in Section 5.3, the orbital motion of the planet is not needed to describe the light curve. Assuming a static lens system, the best-fit values of the planet/star mass ratio and normalized star–planet separation are $q = 5.425 \times 10^{-5}$ and $s = 0.91422$, respectively. The values of other lensing parameters are listed in Table 2. This table also lists the best-fit parameters for fits including orbital motion. The inclusion of orbital motion improves χ^2 by $\Delta\chi^2 = 3.24$ for 2 fewer degrees of freedom, but it also changes the planet/star mass ratio and normalized star–planet separation to $q = 5.815 \times 10^{-5}$ and $s = 0.91429$. As discussed below in Section 5.4, the inclusion of microlensing parallax adds a parameter degeneracy that takes $u_0 \to -u_0$ and $\theta \to -\theta$, which corresponds to a reflection of the lens plane with respect to the geometry of Earth's orbit. We find that the model with $u_0 > 0$ is favored by $\Delta\chi^2 = 13.39$ for static models and $\Delta\chi^2 = 6.31$ for models with orbital motion. The χ^2 contribution of the individual data sets for the best models with and without orbital motion is shown in Table 1. We note that this mass ratio is the lowest of planets yet to be discovered by the microlensing method.

Figure 1 shows the best-fit model curve compared to the light curve data. Figure 5 compares the planetary caustic geometry to the source size and trajectory. The two triangular-shaped
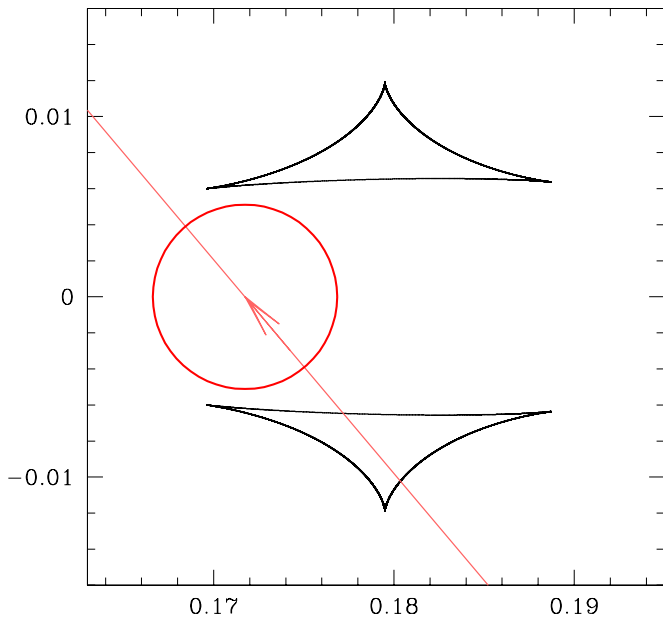
Figure 5. Planetary caustic for the best-fit MOA-2009-BLG-266 light-curve model is shown in black. The red circle indicates the size of the source star and the red line indicates its trajectory. The coordinates are in Einstein radius units with the center of mass at the origin.

Table 3
Physical Parameters

Parameter	Units	Value	2σ Range
D_L	kpc	3.04 ± 0.33	2.4–3.7
$M_\star$	$M_\odot$	0.56 ± 0.09	0.39–0.74
m_p	$M_\oplus$	10.4 ± 1.7	7.2–14
a	AU	$3.2^{+1.9}_{-0.5}$	2.3–13
P	yr	$7.6^{+7.7}_{-1.4}$	5.4–62

Notes. Uncertainties are 1σ parameter ranges.

caustics indicate a minor image caustic perturbation, which is seen when the star–planet separation is less than the Einstein radius ($s < 1$). The strongest feature in such a minor image caustic crossing event is the large decrease in magnification at HJD $\sim 2{,}455{,}086.5$ when the source is between the caustics and the minor image is essentially destroyed. This feature is surrounded by two positive light curve bumps caused by the source passing over a caustic or passing in front of the cusps. There are no known non-planetary light curve perturbations that can produce such a feature in the light curve (Gaudi & Gould 1997). For MOA-2009-BLG-266, the local light curve minimum between the caustic crossings has a short duration of $\sim$3.7 hr, which is much smaller than the caustic crossing durations of $>$20 hr. This is due to the fact that separation between the two triangular minor image caustics is only slightly larger than the diameter of the source star.

5.3. Orbital Motion

Like most low-mass planetary microlensing events, MOA-2009-BLG-266 can be modeled well without including any orbital motion of the planet about the host star. But, while we have not measured the light curve precisely enough to measure orbital motion parameters, the planetary orbital motion does influence the precision to which the parameters can be measured from the light curve. In particular, orbital motion allows the planetary caustic to move with respect to the center of mass of the system. Thus, the planetary caustic can be either larger or smaller than the value determined from static lens models, so the mass ratio is not measured as precisely as the static models would imply. In addition, the source radius crossing time is also determined by the time it takes the source to cross the sharp light curve features of the planetary caustic, so this also depends on the orbital motion of the planet and is less precisely determined than the static models would imply.

We include orbital motion using the parameterization used for the analysis of the two-planet event OGLE-2006-BLG-109Lb,c (Bennett et al. 2010), with the x-axis defined by the vector

separating the star and planet at HJD $= 2{,}455{,}086$. The main orbital motion parameters are $\dot{s}_x$ and $\dot{s}_y$, which describe the instantaneous planet velocity at the time HJD $= 2{,}455{,}086$. This parameterization also includes the orbital period, $T_{\rm orb}$, but this parameter has a very small effect on the χ^2 value if it is in the range of physically reasonable values. So, for many of our calculations, we have left $T_{\rm orb}$ fixed at a physically reasonable value. Independent calculations with a slightly different orbital motion parameterization (Skowron 2011) reached identical conclusions.

The effect of the orbital motion on the other light curve parameters can be seen in Table 2, which shows the parameters and error bars for models with and without orbital motion. The inclusion of orbital motion shifts the values of q and $t_\star$ significantly, by 2.6 and 3.8 times the error bars of the static solution, respectively. Orbital motion also increases the error bar on q by a factor of 3.6 and the error bar on $t_\star$ by a factor of 5.7, but the error bars on the other parameters do not change significantly, except for the error bar on t_0, which grows by a factor of 1.6. The error bars on the implied physical parameters, shown in Table 3, also do not change very much when orbital motion is included. However, the central values of the physical parameters do change by as much as 0.4σ.

While the light curve has not been measured precisely enough to significantly constrain the orbital motion, the orbital motion can be constrained with the requirement that the planet be bound to its host star. Such a constraint requires that the mass and distance of the host star be known, but the light curve does provide this information as shown below in Equations (13) and (14). The light curve parameters include the transverse host-star–planet separation, s, and the transverse components of the planet velocity, $\dot{s}_x$ and $\dot{s}_y$. One option is to enforce a model constraint that the orbital motion parameters are consistent with a physical circular orbit. This is equivalent to imposing a constraint on the distance to the source (Bennett et al. 2010). We take this limit to be $D_S = 8.8 \pm 1.2$ kpc, which is somewhat larger than the measured scatter of the distance of bulge clump giant stars at the Galactic longitude of this event (Rattenbury 2007) because we do not wish to enforce the circular orbit model too strictly. This constraint has been employed for the best-fit model shown in Table 2. But, such a constraint is inconvenient to use in our MCMC calculations to determine the distribution of allowed light curve and physical parameters, as it makes it more difficult to obtain well-sampled Markov Chains.

A slightly weaker, but more general, constraint can be obtained by requiring that the orbital velocity not be too large to allow the planet to be gravitationally bound to the star, since the probability of lensing by a planet not bound to the lens star is $\lesssim 10^{-8}$. The transverse velocity components allow us to compute lower limits on the planetary kinetic energy and gravitational binding energy (or an upper limit on the absolute

value of the binding energy). The requirement that the total energy < 0 yields an upper limit on the transverse planet velocity (Dong et al. 2009b):

$$\dot{s}_x^2 + \dot{s}_y^2 \leqslant \frac{2GM_L}{d_\perp R_E^2} = \frac{2GM_L}{s(\theta_E D_L)^3} \qquad (11)$$

where $d_\perp$ is the transverse star–planet separation. The $R_E^3 = (\theta_E D_L)^3$ factor in the denominator is needed because the planet–star separation, s, and transverse velocity components use the Einstein radius as their unit of length.

The constraint, Equation (11), has been used in all of our MCMC calculations to determine the allowed parameter distributions, and we have also added a $\Delta\chi^2 = 4$ penalty to potential MCMC links with $\dot{s}_x^2 + \dot{s}_y^2$ of more than half the upper limit in Equation (11). Such parameter sets are unlikely because they require a kinetic energy higher than the average value and small values for the separation and velocity along the line of sight. Attempts to find best solutions with the Equation (11) in place of the circular orbit, source distance constraint did not yield better solutions than the one shown in Table 2.

5.4. The Parallax Effect

The microlens parallax is defined by the ratio of Earth's orbit to the physical Einstein radius projected on the observer plane, $\tilde{r}_E$, i.e.,

$$\pi_E = \frac{AU}{\tilde{r}_E}. \qquad (12)$$

Lens parallaxes are usually measured from the deviation of the light curve from those of standard (single or binary) lensing events due to the deviation of the source trajectory from a straight line caused by the orbital motion of the Earth around the Sun (Gould 1992; Alcock et al. 1995). But it is also possible to detect microlensing parallax using observations from a spacecraft in a heliocentric orbit (Refsdal 1966; Dong et al. 2007), and such satellite observations have the potential to significantly increase the number of events for which the microlensing parallax effect may be detected.

For the event MOA-2009-BLG-266, the parallax effect is firmly detected. We find that the χ^2 difference between the (static) best-fit models with and without the parallax effect is $\Delta\chi^2 = 2789.3$, which implies that microlensing parallax is detected at the $\sim 53\sigma$ level. The difference between the parallax and non-parallax models can be seen in Figure 1, where the best-fit model is plotted as a solid black curve and the best-fit non-parallax model is the gray dashed curve. Most of the parallax signal comes from the data outside of the planetary deviation. The light curve without parallax lies below the observed data prior to the planetary perturbation and above the data after the light curve peak. Most of the signal comes from the MOA data, but good coverage of the global light curve shape from CTIO and Canopus has enabled these light curves to contribute to the parallax signal.

There are a number of degeneracies that often affect the parallax parameters of an event. For events with parallax effect, a pair of source trajectories with the impact parameter and source trajectory angle of (u_0, θ) and $(-u_0, -\theta)$ can yield degenerate solutions (Smith et al. 2003). Without parallax, this transformation is a trivial redefinition of parameters, but with parallax, we have the reference frame of Earth's orbit, which allows us to distinguish between two solutions that differ by a reflection of the lens plane. For single-lens events

with t_E as small as ~ 60 days, there is usually an additional degeneracy known as the jerk-parallax degeneracy (Gould 2004), but the additional light curve structure due to the planet removes some of the parameter degeneracy. As a result, the $(u_0, \theta) \leftrightarrow (-u_0, -\theta)$ degeneracy and the jerk-parallax degeneracy are replaced by a single-parameter degeneracy that makes the $(u_0, \theta) \leftrightarrow (-u_0, -\theta)$ and changes the parallax parameter, $\boldsymbol{\pi}_E$. This degeneracy yields the two solutions with similar parameters, but when orbital motion of the planet is ignored, there are significant differences in the other model parameters besides u_0 and θ. With no orbital motion, the $u_0 > 0$ solution is favored by $\Delta\chi^2 = 13.39$. Formally, this is quite significant as the $u_0 < 0$ solution would be disfavored by a formal probability of $e^{-\Delta\chi^2/2} \approx 0.0012$, but we must also consider possible systematic errors that may influence the $\Delta\chi^2$ value between the $u_0 > 0$ and $u_0 < 0$ solutions, as well as the orbital motion of the planet.

This concern about possible systematic errors was the reason for the careful limb-darkening treatment described in Section 4.3. In addition, we also considered a number of different photometric reductions of the data sets that contribute the most to the detection of the parallax signal. These were the MOA, Canopus, and CTIO I- and H-band data sets. With these different photometric reductions, we found that the $u_0 > 0$ solution was always favored by a similar $\Delta\chi^2$ difference, although the SoDoPHOT reduction of the CTIO I-band data set and the DoPHOT reduction of the CTIO H-band data set favored the $u_0 < 0$ solution by a somewhat larger $\Delta\chi^2$ difference. Table 1 indicates that the χ^2 difference between the $u_0 > 0$ and $u_0 < 0$ solutions is spread over a number of different data sets.

The inclusion of the orbital motion parameters discussed in Section 4.3 has a significant effect on the $(u_0, \theta) \leftrightarrow (-u_0, -\theta)$ degeneracy. When the orbital motion parameters are included, the best-fit $(u_0 > 0)$ model improves its χ^2 value by $\Delta\chi^2 = 3.24$, but the χ^2 improvement for the $u_0 < 0$ models is even greater, $\Delta\chi^2 = 10.34$, so that the χ^2 difference between the $u_0 < 0$ and $u_0 > 0$ solutions drops to $\Delta\chi^2 = 6.29$ when the planetary orbital motion parameters are included in the models. But an even more significant difference is that the differences between the other parameters for these degenerate models largely disappear when orbital motion is included. The added degrees of freedom provided by the orbital motion parameters appear to be larger than the light curve difference enforced by the $(u_0, \theta) \leftrightarrow (-u_0, -\theta)$ transformation. As a result, once orbital motion is included, the $(u_0, \theta) \leftrightarrow (-u_0, -\theta)$ degeneracy has no obvious effect on the determination of the physical parameters of the event.

Figure 6 shows the distribution of parallax parameters, $(\pi_{E,N}, \pi_{E,E})$, or equivalently, (π_E, ϕ_E), found by our MCMC simulations. This plot includes 11 separate MCMC chains with a total of 593,000 links as discussed in Section 5.5. The distributions for both solutions are highly elongated along the $\pi_{E,N}$ axis. This is due to the fact that Earth's acceleration is almost entirely in the east–west direction, when projected on the plane perpendicular to the line of sight to the Galactic bulge. Figure 6 also shows contours of constant π_E, which are labeled by the (approximate) corresponding lens mass. The lens mass depends on the angular Einstein radius, which our MCMC calculations determine to be $\theta_E = 0.98 \pm 0.04$ mas. However, these mass contours in Figure 6 are only approximate because they do not include any correlations between the π_E and θ_E values. These correlations are properly incorporated
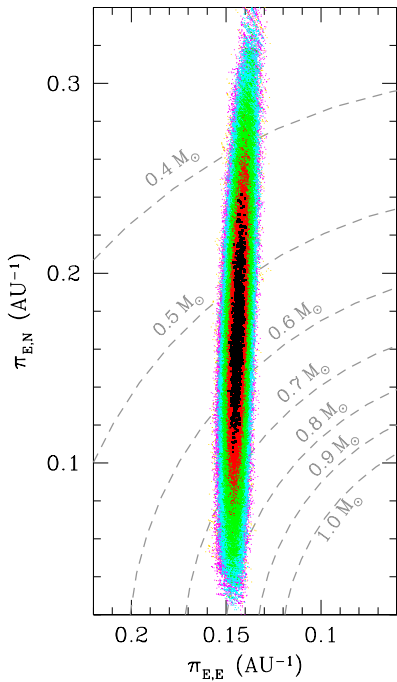
Figure 6. Distribution of the microlensing parallax vector $\boldsymbol{\pi}_E = (\pi_{E,N}, \pi_{E,E})$ values that are consistent with the observed light curve taken from our MCMC runs in the regions of the two local χ^2 minima with $u_0 < 0$ and $u_0 > 0$. The points are color coded based on their difference from the χ^2 minimum of 6050.2, with points with $\Delta\chi^2 \leqslant 1, 4, 9, 16, 25, 36$, and $\Delta\chi^2 > 36$ represented by black, red, green, cyan, magenta, and gold dots, respectively. The gray dashed circles indicate contours of constant $\pi_E = 1/\tilde{r}_E$ and therefore (approximately) constant mass. These assume the mean angular Einstein radius from our MCMC calculations, $\theta_E = 0.985$ mas.

into our MCMC calculations, which yield the host star and planet masses, $M_\star = 0.56 \pm 0.09\,M_\odot$ and $m_p = 10.4 \pm 1.7\,M_\oplus$, located at a distance of $D_L = 3.04 \pm 0.33$ kpc. Assuming a random orientation of the orbit, we estimate a semimajor axis of $a = 3.2^{+1.9}_{-0.5}$ AU. If we assume a standard position for the snow line, $\sim 2.7(M/M_\odot)$ AU (Kennedy & Kenyon 2008), then the planet orbits at about twice the distance of the snow line, similar to the position of Jupiter in our own solar system. Thus, the planet might be considered to be a "failed Jupiter" core as predicted by the core accretion theory (Thommes et al. 2008; Ida & Lin 2005), in which the rock–ice core only reaches $\sim 10\,M_\oplus$ after the hydrogen and helium gas in the protoplanetary disk has dissipated.

In principle, any orbital parallax signal can be mimicked by the so-called xallarap, i.e., orbital motion of the source about a companion (Griest & Hu 1992; Han & Gould 1997). However, this would require very special orbital parameters, basically mimicking those of the Earth (Smith et al. 2002). We search for such xallarap solutions over circular orbits, i.e., with three additional free parameters (orbital phase, inclination, and period). We find a χ^2 improvement of 3.9 relative to the parallax solution for 3 degrees of freedom, or 3.4 with the period fixed at $P = 1$ yr (2 degrees of freedom). These improvements have no statistical significance and are to be compared with the improvement of $\Delta\chi^2 = 2789.3$ for the parallax solution relative to the no-parallax solution. Therefore, we conclude that the light curve distortions are due to parallax rather than xallarap (Poindexter et al. 2005).

Our final fit parameters are listed in Table 2. The parameters $\pi_{E,N}$ and $\pi_{E,E}$ are the north and east components of the

microlensing parallax vector, $\boldsymbol{\pi}_E$. The uncertainty in $\pi_{E,N}$ is an order of magnitude larger than the uncertainty in $\pi_{E,E}$ because the projected acceleration of the Earth is largely in the east–west direction during this event.

5.5. Parameter Uncertainties

Uncertainties in the parameters have been determined by a set of 11 MCMC runs with a total of approximately 593,000 links. Eight of these MCMC runs have been in the vicinity of the $u_0 > 0$ solution and the other three have been in the vicinity of the $u_0 < 0$ local χ^2 minimum. Due to the χ^2 difference, $\Delta\chi^2 = 6.29$ between these local χ^2 minima, we include a weight factor to our sums over the Markov chains so that the disfavored $u_0 < 0$ solutions are disfavored by an amount appropriate for their χ^2 difference, $e^{-\Delta\chi^2} = 0.043$. The mean parameter values for these solutions and their uncertainties are shown in Table 2. For most parameters, these are given by the weighted averages over the 11 Markov chains, but for u_0 and θ, we have included only the 8 Markov chains with $u_0 > 0$ and $\theta > 0$. Due to the large difference in these parameters in the vicinity of the two solutions, the mean values would be values that are inconsistent with both solutions if we had used both solutions for these sums. For the remaining parameters, except $\dot{s}_x$ and $\dot{s}_y$, the parameter distributions for the vicinities of the two local χ^2 minima are nearly identical.

5.6. Physical Parameters

The source radius crossing time, $t_\star$, is an important parameter because it helps to determine the angular Einstein radius, $\theta_E = \theta_\star t_E/t_\star$, as discussed in Section 4.2. When this is combined with the measurement of the microlensing parallax signal, we are able to determine the mass of the lens system (Gould 1992),

$$M_L = \frac{\theta_E c^2 \mathrm{AU}}{4G\pi_E} = \frac{\theta_E}{(8.1439\,\mathrm{mas})\pi_E}M_\odot \approx 0.57\,M_\odot, \quad (13)$$

if we assume that the favored parameters of the best-fit ($u_0 > 0$) solution are correct. The lens system distance can also be determined as

$$D_L = \frac{\mathrm{AU}}{\pi_E\theta_E + \pi_S} \approx 3.2\,\mathrm{kpc}, \quad (14)$$

assuming that the distance to the source, $D_S = 1/\pi_S$, is known. Note that these values from the best-fit solution are not identical to the central values from our full MCMC analysis, although they are very close.

In order to determine the physical parameters of this planetary lens system, it is important to include the effects of correlations of the parameters and the uncertainties in external measurements, such as the determination of $\theta_\star$. Such a calculation is easily done with MCMC simulations. As discussed in Sections 5.4 and 5.5, we have run 11 MCMCs in the vicinity of both the degenerate $u_0 > 0$ and $u_0 < 0$. The distribution of the parallax parameters for these solutions is shown in Figure 6. The gray dashed circles in this figure show the contours of constant π_E, which correspond to contours of constant mass by Equation (13). However, this correspondence is only approximate because θ_E is slightly correlated with π_E.

These MCMC simulations can also be used to determine the physical parameters of the host star and its planet, which are summarized in Table 3. This is essentially a Bayesian analysis, but the only non-trivial prior that we impose is the

assumption that the orbital orientation is random, which is used to estimate the semimajor axis, a, based on the measured two-dimensional separation in the plane of the sky. If planets are much more common at very small or very large separations, then the planetary detection would imply a bias that violates this assumption. However, the available evidence indicates that planet frequency does not have a sharp dependence on the semimajor axis, so this assumption seems reasonable. Our MCMC calculations assumed a fixed distance of 8.8 kpc to the source star, due to its position on the more distant end of the Galactic bar. We have adjusted the uncertainties in Table 3 to include the 5% spread in the distance to bulge clump stars measured in this direction (Rattenbury 2007; although the effect is quite small.) The probability distributions for the host star and planet masses and distance ($M_\star$, m_p, and D_L) are nearly Gaussian, so they are described well simply by their mean values and dispersions. This is not the case for our estimate of the semimajor axis, a, which has a 2σ (95% confidence level) range of 2.3–12.9 AU.

We therefore conclude that the MOA-2009-BLG-266Lb planet is a $\sim 10\,M_\oplus$ planet at a separation of ~ 3 AU. In the core accretion model of planet formation, the snow line is an important location where the density of solid material jumps by about a factor of five due to the condensation of ices (mostly water ice; Ida & Lin 2005; Lecar 2006; Kennedy et al. 2006; Kennedy & Kenyon 2008; Thommes et al. 2008). Assuming a standard position for the snow line, $\sim 2.7(M/M_\odot)$ AU, we find that the planet is located at about twice the distance of the snow line, similar to the position of Jupiter in our own solar system. It is therefore a prime candidate to be a "failed Jupiter core," which grew by the accumulation of solid material to $\sim 10\,M_\oplus$, but was unable to grow into a gas giant by the accretion of hydrogen and helium because the protoplanetary disk had lost its gas before the planetary core was massive enough to accrete it efficiently.

The mass measurements of the planet and host star given in Table 3 have uncertainties of about 16%, which is dominated by the uncertainty in $\pi_{E,N}$. This uncertainty can be reduced to 5–10 yr, hence when the source and planetary host stars have separated enough to allow their relative proper motion to be measured (Bennett et al. 2007). Since π_E is parallel to the lens–source proper motion, this will reduce the uncertainty in π_E to a value much closer to the 2.4% uncertainty in $\pi_{E,E}$, which should reduce the uncertainties in the star and planet masses to $<5\%$. Our existing VLT/NACO observations indicate that the combined H-band flux of the source and host star is $H = 13.77 \pm 0.05$, which is consistent with our prediction that the host star should be ~ 75 times fainter than the source and indicate no neighbor stars that might interfere with the detection of the source–host-star relative motion. Therefore, we expect that it will be feasible to improve these mass measurements in the future.

We find a host star of mass $M_\star = 0.56 \pm 0.09\,M_\odot$ orbited by a planet of mass $m_p = 10.4 \pm 1.7\,M_\oplus$, located at a distance of $D_L = 3.04 \pm 0.33$ kpc. Assuming a random orientation of the orbit, we estimate a semimajor axis of $a = 3.2^{+1.9}_{-0.5}$ AU and an orbital period of $P = 7.6^{+7.7}_{-1.4}$ yr. If we assume a standard position for the snow line, $\sim 2.7(M/M_\odot)$ AU (Kennedy & Kenyon 2008), as indicated in Figure 7, then the planet orbits at about twice the distance of the snow line, similar to the position of Jupiter in our own solar system. However, the planet's mass of $\sim 10\,M_\oplus$ is close to the critical mass predicted by core accretion theory (Thommes et al. 2008) where it has
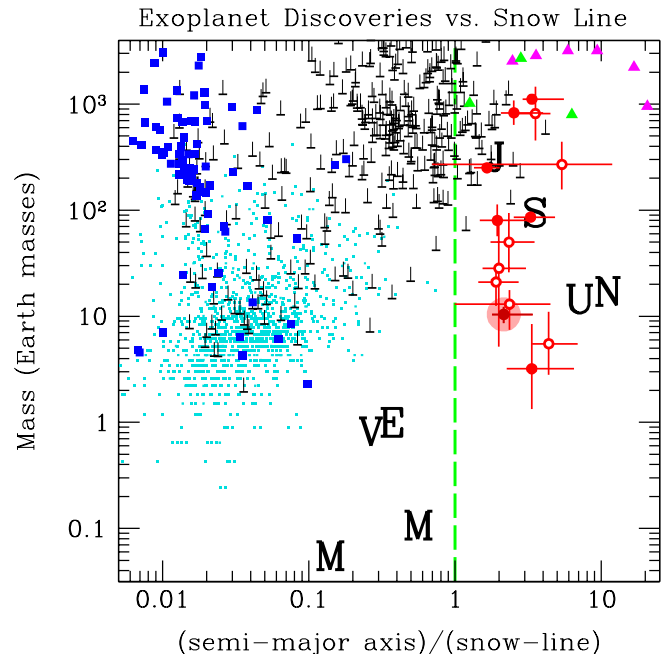

Figure 7. Masses of the known exoplanets are shown as a function of their semimajor axis divided by the snow line, which is assumed to depend on the host star mass as $\sim 2.7 M/M_\odot$ AU. Red error-bar crosses indicate microlensing discoveries, with MOA-2009-BLG-266Lb indicated by the dark red spot surrounded by the light red halo. The black, upside down "T"s and blue squares indicate exoplanets discovered by the radial velocity and transit methods, and the magenta and green triangles are planets discovered by imaging and timing. The small cyan dots are planet candidates found by *Kepler*, but not yet validated or confirmed (using the mass radius relation of Traub 2011). The microlensing planets indicated by open circles have had their masses and semimajor axes estimated by a Bayesian statistical analysis.

exhausted the nearby supply of solid material and begins the slow, quasistatic gas accretion phase. So, MOA-2009-BLG-266Lb fits the theoretical predictions for a large population of "failed gas giant" core (Laughlin et al. 2004) planets, which would have had their growth terminated by the loss of gas from the protoplanetary disk prior to the rapid gas accretion phase. Indeed, the distribution of planets found by microlensing, shown in Figure 7, seems to confirm this prediction, as the detection efficiency corrected planetary mass function rises steeply, as $\sim q^{-0.7 \pm 0.2}$ toward lower mass ratios (Sumi et al. 2010). However, a much sharper comparison to theory can be made with mass measurements of these planets and their host stars. Some theoretical treatments suggest a relatively sharp feature in the mass function at $\sim 10\,M_\oplus$, and the low-mass end of the exoplanet mass function is likely to depend on the host star mass. MOA-2007-BLG-192Lb (Kubas et al. 2011) is the only other cold, low-mass planet with a host star mass measurement, but the planet mass is weakly constrained due to a poorly sampled light curve.

6. CONCLUSIONS AND IMPLICATIONS FOR FUTURE DISCOVERIES

Figure 7 shows the distribution of known exoplanets as a function of mass and separation, with the separation given in units of the snow line, which is estimated to be located at $\sim 2.7\,M/M_\odot$ AU (Ida & Lin 2004; G. M. Kennedy 2008, private communication). (We correct the Ida & Lin formula to use scale with the stellar luminosity at the time of planet formation, $\sim 10^6$ yr, instead of the main-sequence luminosity.) The small

cyan dots in this plot indicate the location of the ∼1200 planet candidates recently announced by the *Kepler* mission (Borucki et al. 2011). However, these planet candidates have only radius estimates and no mass estimates, so we estimate their masses using the mass–radius formula of Traub (2011).

While there are a number of exoplanets found by microlensing with similar mass and separation, MOA-2009-BLG-266Lb is the only low-mass planet from microlensing with a precisely measured mass. MOA-2007-BLG-192Lb is likely to be the lowest mass planet, at ∼3 $M_\oplus$, found by microlensing (Bennett et al. 2008; Kubas et al. 2011), and the mass of the host star has been reasonably well determined, $0.084^{+0.015}_{-0.012}$ $M_\odot$ due to a microlensing parallax signal and detection of the host star in high-resolution AO images. However, the event was not alerted until the planetary signal was over, and as a result, the planetary light curve is poorly sampled. This results in an uncertain planetary mass ratio, so that the mass is not precisely measured.

Current and future developments in the microlensing field suggest that such mass measurements may become much more common in the near future. The rate of microlensing planet discoveries is expected to increase significantly in the near future, with the high-cadence, wide-field approach of MOA-II being adopted by a number of other observing programs, such as the OGLE-IV and Wise Observatory surveys, which should begin full operations in 2011 and 2012, respectively. The most ambitious ground-based program, the Korean Microlensing Telescope Network (KMTNet) is expected to follow a few years later (Kim et al. 2010). The observations from the *EPOXI* spacecraft have made only a modest contribution to this discovery, due to the limited observing time and relatively small distance (∼0.1 AU) from Earth. But future observations from *EPOXI* or other solar system exploration spacecraft at a more typical separation of ≳1 AU would be much more effective, and will be able to determine masses for most of the events that they observe. Finally, follow-up images with the *Hubble Space Telescope* will enable mass determinations of many of the planets discovered by microlensing, after a few years of lens–source relative proper motion (Bennett et al. 2007). The results presented here illustrate that it will often be possible to precisely determine the host star and planet masses and so measure the mass function of cold planets in the Earth–Jupiter mass range as a function of their host mass, which together with the Doppler and transit methods will provide crucial constraints on the physics of planet formation across the wide range of planet/star separations.

This discovery tends to confirm the earlier claims (Sumi et al. 2010; Gould et al. 2010) that microlensing has revealed a previously undetected population of cold, relatively low-mass planets, and the measurement of the planet and host star masses suggests that this population of planets may be related to the "failed Jupiter-cores" predicted by the core accretion theory, although there are alternative mechanisms that could form such planets (Boss 2006). Microlensing observations could provide much sharper tests of these theories if there were more discoveries with precisely measured masses.

One potentially promising avenue for such measurements is further observations with small telescopes on solar system exploration spacecraft, such as we have obtained with *EPOXI*. While the *EPOXI* observations of MOA-2009-BLG-266 have made only a modest contribution to the microlensing parallax measurement, this is a consequence of the poor light-curve coverage of the *EPOXI* observations and the close proximity of *EPOXI* to Earth (∼0.1 AU) at the time of observations. Observations from *EPOXI* or a similar spacecraft at a more typical (≳1 AU) distance, with better light-curve coverage (as might be obtained during an extended mission) would be very effective at measuring lens masses. Furthermore, such a spacecraft could measure masses for planets and their host stars residing in the Galactic bulge, which is probably the case for OGLE-2005-BLG-390Lb (Beaulieu et al. 2006) and MOA-2008-BLG-310Lb (Janczak et al. 2010). These events have such short timescales that the orbital motion of the Earth is very unlikely to allow the measurement of the microlensing parallax, but in most cases, a telescope in a heliocentric orbit at ≳1 AU will be able to measure the microlensing parallax effect and determine the planet and host star masses.

Of course, the study of low-mass planets beyond the snow line would benefit greatly from an increased discovery rate over the current rate of ∼4 yr^{-1}. The original strategy for finding planets by microlensing (Mao & Paczyński 1991; Gould & Loeb 1992) was to have one wide FOV telescope identifying microlensing events that are then observed by a global network of narrow FOV follow-up telescopes. This strategy was developed in 1992 and was expected to find Jupiter-mass planets in Jupiter-like orbits. It has proved to be not very efficient for lower mass planets, although some important discoveries have been made (Beaulieu et al. 2006).

The development of the high-magnification strategy (Griest & Safizadeh 1998; Rhie et al. 2000) led to a significant increase in observing efficiency because, while high-magnification planetary signals are rare compared to low-magnification planetary signals, the detection efficiency during the brief period of high magnification is extremely high. Also, small telescopes can perform precise photometry at high magnification. Thus, a substantial fraction of the planet microlensing planet discoveries to date have come from high-magnification events (Gould et al. 2010).

However, even when this high-magnification strategy is adopted, the vast majority of the ∼700 microlensing events observed per year are not effectively monitored for planetary signals. It is simply impossible to obtain precise photometry on so many events using narrow FOV telescopes. In order to improve the planetary discovery event rate, it is necessary to monitor the entire bulge with a high enough cadence so that planetary signals can be detected in all of the observed microlensing events, even those without a high planet detection efficiency. There are so many of these low-efficiency events that they will dominate the total planet detection efficiency when they can all be monitored.

The MOA-II survey is the first microlensing survey with a large enough FOV for a high-cadence survey. The ∼2.2 deg^2 MOA-II telescope FOV is able to observe 13 deg^2 of the central Galactic bulge every 15 minutes, another 13 deg^2 of somewhat lower priority bulge fields every 47 minutes, and 18 deg^2 of outer bulge fields every 95 minutes. This has enabled the survey detection of five planets to date: MOA-2007-BLG-192Lb (Bennett et al. 2008), OGLE-2007-BLG-368Lb (Sumi et al. 2010), and MOA-2009-BLG-266Lb presented here, plus two additional events from the 2010 season that are under analysis. These events (except for MOA-2007-BLG-192) required detection in real time in order to obtain good coverage of the planetary anomaly.

We expect the rate of these survey discoveries to increase quite rapidly in the near future as the number of telescopes involved in these high-cadence surveys is increasing quite rapidly. The OGLE-IV survey with a 1.4 deg^2 camera has just begun on

the OGLE 1.3 m telescope in Las Campanas, Chile. Although OGLE-IV has a smaller telescope and FOV than MOA-II, it has better seeing, and so it should have higher planet detection sensitivity. Nearly complete longitude coverage should also be possible for part of the season as a group from Tel-Aviv University is beginning a dedicated Galactic bulge monitoring program with a $1.0\,deg^2$ imager on the 1.0 m telescope at Wise Observatory in Israel in 2011 after a six-week pilot program in 2010.

The most ambitious project is KMTNet (Kim et al. 2010), which is building a network of three 1.6 m telescopes equipped with $4.0\,deg^2$ cameras in South Africa, (northern) Chile, and Australia. The KMTNet system will have the capability for continuous coverage of all bulge microlensing events by itself, when the weather permits, but it is also locating its telescopes at different sites from the existing MOA-II, OGLE-IV, and Wise telescopes, so that complete light-curve coverage will often be possible when some sites have bad weather. This should result in a significant increase in the rate of microlensing planet discoveries.

REFERENCES

Alard, C., & Lupton, R. H. 1998, ApJ, 503, 325
Albrow, M. D. 2000, ApJ, 534, 894
Albrow, M. D., Horne, K., Bramich, D. M., et al. 2009, MNRAS, 397, 2099
Alcock, C., Allsman, R. A., Alves, D., et al. 1995, ApJ, 454, L125
Baraffe, I., Chabrier, G., Barman, T. S., et al. 2005, A&A, 436, L47
Barry, R. K., Lindler, D., Deming, L. D., et al. 2010, Proc. SPIE, 7731, 77313
Batista, V., Gould, A., Dieters, S., et al. 2011, A&A, 529, A102
Beaulieu, J.-P., Bennett, D. P., Fouqué, P., et al. 2006, Nature, 439, 437
Bennett, D. P. 2008, in Exoplanets, ed. J. Mason (Berlin: Springer), 47
Bennett, D. P. 2010, ApJ, 716, 1408
Bennett, D. P., Alcock, C., Allsman, R., et al. 1993, BAAS, 25, 1402
Bennett, D. P., Anderson, J., & Gaudi, B. S. 2007, ApJ, 660, 781
Bennett, D. P., Bond, I. A., Udalski, A., et al. 2008, ApJ, 684, 663
Bennett, D. P., & Rhie, S. H. 1996, ApJ, 472, 660
Bennett, D. P., Rhie, S. H., Nikolaev, S., et al. 2010, ApJ, 713, 837
Bond, I. A., Abe, F., Dodd, R. J., et al. 2001, MNRAS, 327, 868
Bond, I. A., Udalski, A., Jaroszyński, M., et al. 2004, ApJ, 606, L155
Borucki, W. J., et al. 2011, ApJ, 736, 19
Boss, A. P. 2006, ApJ, 644, L79
Bramich, D. M. 2008, MNRAS, 386, L77
Cardelli, J. A., Clayton, G. C., & Mathis, J. S. 1989, ApJ, 345, 245
Carpenter, J. M. 2001, AJ, 121, 2851
Claret, A. 2000, A&A, 363, 1081
Christiansen, J. L., Ballard, S., Charbonneau, D., et al. 2011, ApJ, 726, 94
Cumming, A., Butler, R. P., Marcy, G. W., et al. 2008, PASP, 120, 531
Dong, S., Bond, I. A., Gould, A., et al. 2009, ApJ, 698, 1826
Dong, S., DePoy, D. L., Gaudi, B. S., et al. 2006, ApJ, 642, 842
Dong, S., Udalski, A., Gould, A., et al. 2007, ApJ, 664, 862
Fruchter, A. S. 2002, PASP, 114, 144
Gaudi, B. S. 2010, in Exoplanets, ed. S. Seager (Tucson, AZ: Univ. Arizona Press), 79
Gaudi, B. S., Bennett, D. P., Udalski, A., et al. 2008, Science, 319, 927
Gaudi, B. S., & Gould, A. 1997, ApJ, 486, 85
Gould, A. 1992, ApJ, 392, 442
Gould, A. 2004, ApJ, 606, 319
Gould, A. 2008, ApJ, 681, 1593
Gould, A., Dong, S., Gaudi, B. S., et al. 2010, ApJ, 720, 1073
Gould, A., & Loeb, A. 1992, ApJ, 396, 104
Gould, A., Udalski, A., An, D., et al. 2006, ApJ, 644, L37
Griest, K., & Hu, W. 1992, ApJ, 397, 362
Griest, K., & Safizadeh, N. 1998, ApJ, 500, 37
Han, C., & Gould, A. 1997, ApJ, 480, 196
Heyrovský, D. 2003, ApJ, 594, 464
Heyrovský, D. 2007, ApJ, 656, 483
Howard, A. W., Marcy, G. W., Johnson, J. A., et al. 2010, Science, 330, 653
Hubickyj, O., Bodenheimer, P., & Lissauer, J. J. 2005, Icarus, 179, 415
Ida, S., & Lin, D. N. C. 2004, ApJ, 604, 388
Ida, S., & Lin, D. N. C. 2005, ApJ, 626, 1045
Janczak, J., Fukui, A., Dong, S., et al. 2010, ApJ, 711, 731
Johnson, J. A., Aller, K. M., Howard, A. W., & Crepp, J. R. 2010, PASP, 112, 905
Kennedy, G. M., & Kenyon, S. J. 2008, ApJ, 673, 502
Kennedy, G. M., Kenyon, S. J., & Bromley, B. C. 2006, ApJ, 650, L139
Kervella, P., Bersier, D., Mourard, D., et al. 2004, A&A, 428, 587
Kim, S. L., et al. 2010, Proc. SPIE, 7733, 77733
Kubas, D., et al. 2011, A&A, in press (arXiv:1009.5665)
Kurucz, R. L. 1993a, Kurucz CD-ROM 16 (Cambridge, MA: SAO)
Kurucz, R. L. 1993b, Kurucz CD-ROM 17 (Cambridge, MA: SAO)
Kurucz, R. L. 1996, in ASP Conf. Ser. 108, Model Atmospheres and Spectrum Synthesis, ed. S. J. Adelman, F. Kupka, & W. W. Weiss (San Francisco, CA: ASP), 2
Laughlin, G., Bodenheimer, P., & Adams, F. C. 2004, ApJ, 612, L73
Lecar, M., Podolak, M., Sasselov, D., & Chiang, E. 2006, ApJ, 640, 1115
Lissauer, J. J. 1993, ARA&A, 31, 129
Mao, S., & Paczyński, B. 1991, ApJ, 374, L37
Miyake, N., Sumi, T., Dong, S., et al. 2011, ApJ, 728, 120
Movshovitz, N., & Podolak, M. 2008, Icarus, 194, 368
Pejcha, O., & Heyrovský, D. 2009, ApJ, 690, 1772
Poindexter, S., Afonso, C., Bennett, D. P., et al. 2005, ApJ, 633, 914
Pollack, J., Hubickyj, O., Bodenheimer, P., et al. 1996, Icarus, 124, 62
Rafikov, R. 2011, ApJ, 727, 86
Rattenbury, N. J. 2007, MNRAS, 378, 1064
Refsdal, S. 1966, MNRAS, 134, 315
Rhie, S. H., Bennett, D. P., Becker, A. C., et al. 2000, ApJ, 533, 378
Sako, T., Sekiguchi, T., Sasaki, M., et al. 2008, Exp. Astron., 22, 56
Schechter, P. L., Mateo, M., & Saha, A. 1993, PASP, 105, 1342
Skowron, J., Udalski, A., Gould, A., et al. 2011, ApJ, 738, 87
Smith, M. C., Mao, S., & Paczyński, B. 2003, MNRAS, 339, 925
Smith, M. C., Mao, S., & Woźniak, P. 2002, MNRAS, 332, 962
Stetson, P. B. 1994, PASP, 106, 250
Stubbs, C. W., High, F. W., George, M. R., et al. 2007, PASP, 119, 1163
Sumi, T., Bennett, D. P., Bond, I. A., et al. 2010, ApJ, 710, 1641
Thommes, E. W., Matsumura, S., & Rasio, F. A. 2008, Science, 321, 814
Tomaney, A. B., & Crotts, A. P. S. 1996, AJ, 112, 2872
Traub, W. 2011, ApJ, submitted
Udalski, A. 2003, Acta Astron., 53, 291
Udalski, A., Jaroszyński, M., Paczyński, B., et al. 2005, ApJ, 628, L109
Udalski, A., Szymanski, M. K., Soszynski, I., & Poleski, R. 2008, Acta Astron., 58, 69
Ward, W. R. 1997, Icarus, 126, 261
Witt, H. J. 1995, ApJ, 449, 42